Integrating Materials and Manufacturing Innovation (2022) 11:172–186
https://doi.org/10.1007/s40192-022-00255-6

TECHNICAL ARTICLE

Computational Alloy Design for Process-Related Uncertainties in Powder Metallurgy

T. T. Molla[1] · A. Atthapreyangkul[1] · G. B. Schaffer[1]

Received: 16 December 2021 / Accepted: 13 February 2022 / Published online: 10 March 2022

Abstract
An integrated computational materials engineering approach to the design of alloys for supersolidus liquid phase sintering has been developed. The method aims to minimize the sensitivity of the alloys to variabilities in material (e.g., composition) and process parameters (e.g., temperature) during sintering while also maximizing mechanical properties. This is achieved by developing a fast acting and high throughput design models that can quantify the processability and the resulting mechanical properties. A highly processable alloy is defined as one that is tolerant to both composition and process conditions such that changes in either do not materially affect the alloy properties. The design models are validated using experimental data from the literature and the computational design approach is demonstrated by designing unique high-speed steels with enhanced processability for powder metallurgy.

Keywords Integrated computational materials engineering (ICME) · Alloy design · High speed steels (HSSs) · Supersolidus liquid phase sintering (SLPS)

Introduction

Several principles guide the design and development of new alloys. One is that an alloy usually requires not one but a set of properties to meet the performance requirements of a component or artefact. Other than bullion, few materials are required to meet a single property goal. A second is that the design is guided by the need to meet the unique requirements of the manufacturing process as much as it is informed by the mechanical and functional property requirements. A key property is thus the processability of the alloy, which can be defined as the sensitivity of the alloy to process and composition variabilities. A highly processable alloy is one that is tolerant to both composition and manufacturing variability such that changes in either will not materially affect the alloy properties. This will serve to reduce cost and increase recyclability, both key properties in themselves. It also appeals to principles of robust functional design as laid out by Taguchi for process control in quality engineering because it reduces the effect of input variation on performance [1].

✉ T. T. Molla
tesfaye.molla@unimelb.edu.au

[1] Department of Mechanical Engineering, The University of Melbourne, Parkville, VIC 3010, Australia

Alloys processed from powders can be particularly sensitive to composition and process related variability [2–8]. A typical example is the limited application of powder metallurgy (PM) involving supersolidus liquid phase sintering (SLPS) to manufacture high speed steels (HSSs) from prealloyed powders [2–6, 9]. SLPS of HSS powders is often challenging because of the difficulties associated with control of the microstructure within a narrow sintering window (i.e., a region in which optimum sintering is realized) [2, 4]. The sintering window in these alloys is controlled by material chemistry and sintering temperature [2]. For instance, small batch to batch differences in feedstock composition of M2 type of HSS may vary the sintering window by about ± 5 K, which is reported to be detrimental for sintering or even makes the powder compact unsinterable [2]. These defects have often hindered the widespread application of PM for processing HSS alloys.

In an attempt to systematically understand the sensitivity of alloys during SLPS, German suggested an analytical approach, based on a hypothetical linear relationship between the composition and the resulting solidus and liquidus temperatures, to incorporate effects of alloy composition into sintering models [9]. On the other hand, Wright et al. used a numerical method, based on the calculation of phase diagrams (CalPhaD), together with experiments,

to investigate the sensitivity of sintering of pre-determined HSS alloys to variations in the concentrations as well as sintering temperature [2]. The methods used by German and Wright et al. can be combined to formulate a fast acting and high throughput alloy design model, which can be used in the framework of Integrated Computational Materials Engineering (ICME) to explore multi-dimensional composition and processing space.

The design of alloys for multiple property requirements via a conventional prototype-and-test protocol is prohibitively time consuming and expensive. The ICME approach can significantly reduce the burden of searching multi-dimensional space and make the problem tractable [10, 11]. We previously reported an ICME framework for designing sintered alloys [12, 13]. Here, we extend the method to demonstrate a computational approach for designing alloys with a reduced sensitivity to variabilities in composition and process parameters (specifically temperature) during sintering while also maximizing mechanical properties. This is achieved by developing a new design model that can quantify the sintering window at high temperature. The approach is demonstrated by designing HSS alloys with the purpose of improving their processability using PM routes. The HSS system is chosen because these alloys are limited by their processability and because the data required for model validation is available in the literature.

Materials System Chart

Following Olson [14], we start with a material systems chart that maps the composition and processing steps to the structure and performance related properties. The material systems chart is a useful guide for systematic optimization because it focusses on the critical factors that determine the structure descriptors which most influence the properties of the material. Because the purpose here is alloy design, we include composition to make it explicit. A chart for powder processed HSS densified by SLPS is shown in Fig. 1. These steels are used in cutting tools and require high yield strength, hardness and wear resistance [15] that are achieved through a combination of primary and secondary carbides in a martensite matrix. In addition, density (porosity) and grain size are structural attributes that also determine the properties. For efficient densification of HSS pre-alloyed powder compacts using SLPS, the structure at the sintering

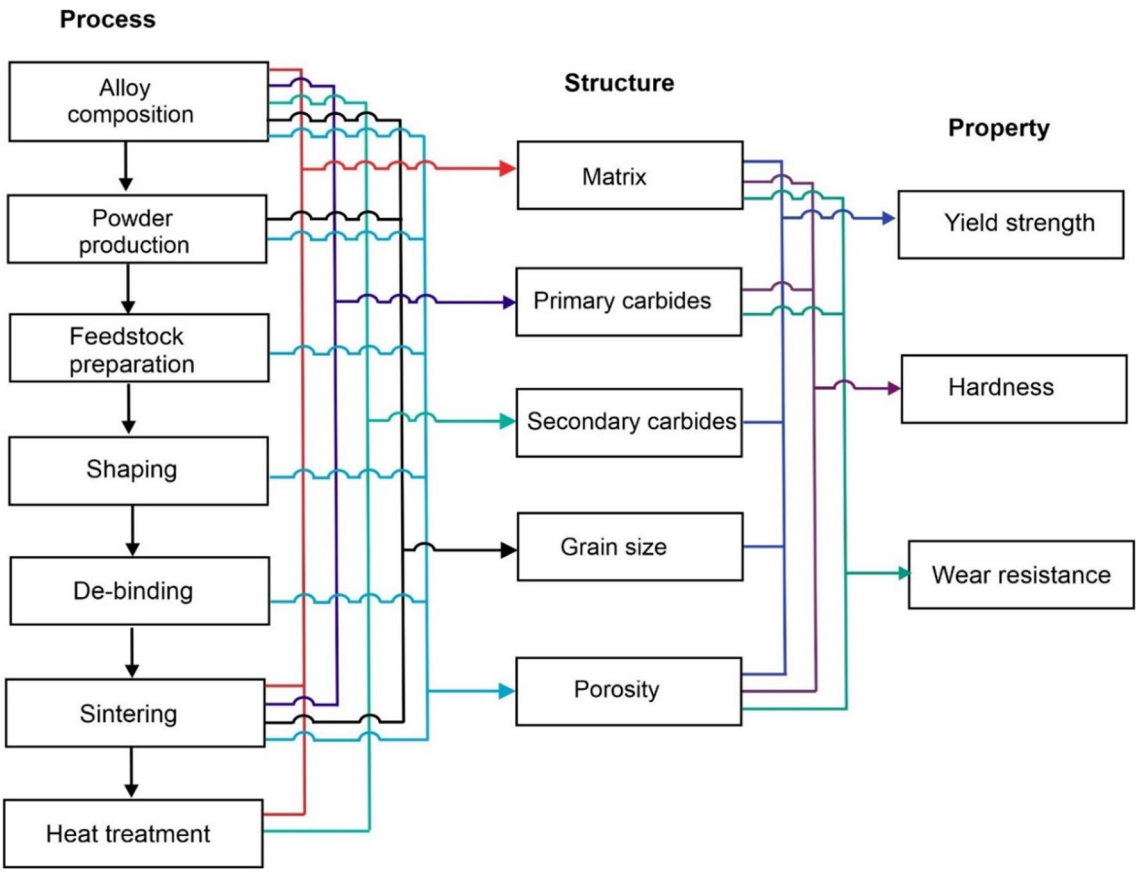

Fig. 1 Materials system chart for HSS alloys processed by PM route

temperature should consist of austenite (FCC), primary carbides (mainly MC and/or M_6C) and liquid (L) phases [2–4]. The critical factors that control the structure and hence properties can be identified by the number of mappings linking the processing step and structural attributes. On this basis, the composition and the sintering step are particularly critical. The search for HSS alloys with enhanced processability through a PM route can thus be performed by optimizing these two critical control factors, composition and sintering temperature. While other factors such as the particle size and particle size distribution also influence the final properties, their effect is largely independent of composition and can therefore be ignored for alloy design purposes.

Design Considerations

According to Wright et al. [3], successful SLPS in HSS powder compacts is affected by certain control factors, which are sensitive to the so-called noise factors. The control factors include alloy composition, sintering temperature and time. The noise factors include batch to batch variation in composition, sintering temperature, particle size distribution and sintering atmosphere. The control factors can desensitize the sintering process from the noise factors and maintain process consistency. Therefore, the design should include criteria that minimize the sensitivity of the alloy to variation in the control factors.

In this study, emphasis is given to the process—structure relationships, i.e., given structural requirements that are known to result in efficient processing, what is the most desirable composition and sintering temperature that realize the structures which are less sensitive to noise factors. Alloy composition is the primary design variable whereas the optimal sintering temperature is determined during the optimization. Below are the microstructural constraints and objectives considered during the development of the computational design method.

Microstructural Constraints

Microstructural Phases at Sintering Temperature

Efficient SLPS of HSS alloys requires that the microstructure at the sintering temperature includes austenite (FCC), metal carbides particularly of M_6C and liquid (L) [2–4]. The liquid phase enhances densification by facilitating grain rearrangement and diffusion while the carbides reduce grain growth. Figure 2 shows a generic phase diagram for HSS alloys indicating the required phase region for efficient SLPS (the sintering window is shown by the shaded area).

By varying the concentration of the alloying elements and the sintering temperature (within pre-defined bounds), a single point phase equilibrium calculation can be used to determine whether a candidate alloy system has the necessary phases for SLPS. This will help to identify alloy systems that will be less likely to over-sinter (i.e., reduction of density during sintering because of microstructural, possibly phase changes) during SLPS. Furthermore, equilibrium calculations can also be used to determine the microstructural phase distribution during solidification of the liquid from the sintering temperature. This is important to identify alloys

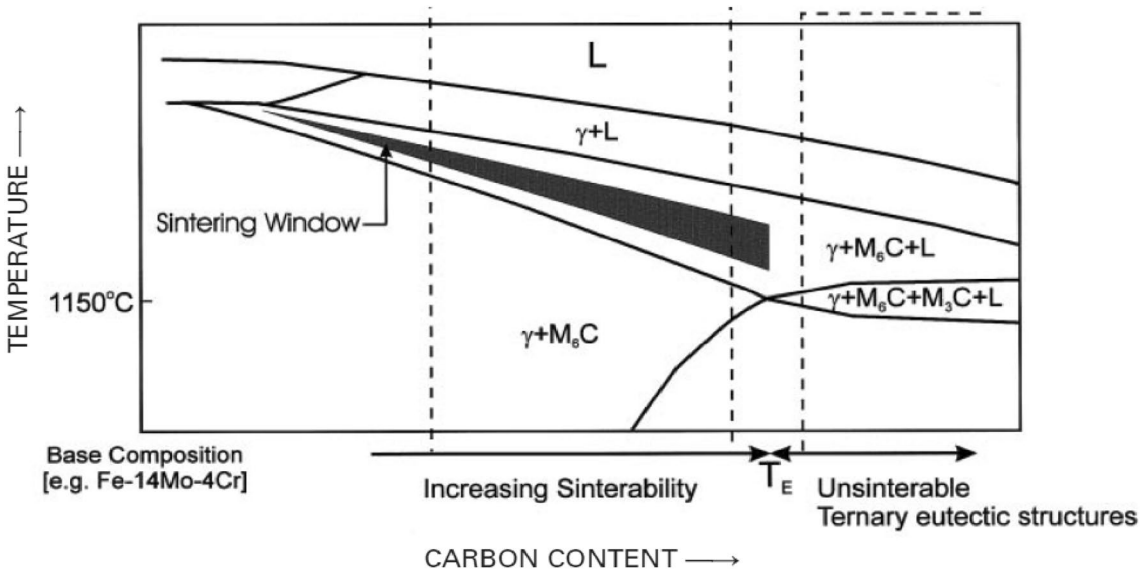

Fig. 2 Schematics showing the generic phase diagram of HSS alloys to describe design objectives meant to improve processability using SLPS [3]

without deleterious phases at room temperature. For example, as shown in Fig. 2, addition of carbon to HSS alloys often results in widening and lowering of the sintering window. However, it may also cause eutectic structures to form during solidification, which are detrimental to the mechanical properties [2].

Amount of Liquid at Sintering Temperature

During SLPS, the liquid is distributed within the grains, between grain boundaries and across interparticle necks [9]. If the grain boundaries within the powder particle are coated with liquid, grain sliding occurs in response to capillary forces. Densification during SLPS is facilitated by grain re-arrangement resulting in particle deformation [5]. This means the capillary force during sintering causes rigid body motion of the grains within the surrounding liquid medium leading to re-arrangement of the grains followed by viscous deformation. A large amount of liquid between the grain boundaries facilitates grain re-arrangement resulting in faster densification but can also cause a loss of rigidity and hence the powder compact may not hold its shape [9]. Thus, the volume fraction of the liquid phase at the sintering temperature is the primary factor that determines the balance between densification and distortion.

The concept of percolation during SLPS can be used to determine the minimum and maximum bounds of the liquid fraction in the microstructure for effective densification without causing defects. German et al. [9] showed that the effect of the liquid phase during SLPS is determined by the fraction of grain boundaries covered by liquid. For equiaxed grains, the fraction of grain boundary covered by liquid, F_c, is given by:

$$F_c = \frac{\mathrm{f}_L\left(1-\mathrm{F}_I\right)R^3}{\delta_L \mathrm{G}^2\left(0.8N_p + 3n_\mathrm{G}\right)} \tag{1}$$

where, f_L is the total fraction of liquid volume in the microstructure, F_I is the fraction of liquid at the grain interior, R is the mean radius of powder particles, G is the average grain size, δ_L is the mean liquid film thickness, n_G is number of grains per particle, and N_p is a factor that depends on the relative density of the compact.

A critical condition occurs when about 80–90% of the grain boundaries are covered by liquid [16]. At this point, the semisolid structure lacks long-range connectivity and densifies by viscous flow. Under optimal circumstances, the body retains slight strength so that densification takes place without distortion. Therefore, assuming F_c between 0.8 and 0.9, it is possible to calculate the range/bound of liquid fraction, f_L for a design optimization depending on the particle radius and grain size in the powder compact. Based on the above analysis, the optimal fraction of the liquid for industrial powder compacts of HSS alloys is found to be in between 10 and 40% [16, 17].

Carbides After Solidification

Solidification of the liquid phase from the sintering temperature affects the amount and type of carbides in the solid phase, which in turn controls the critical performance properties of HSS alloys. Generation of eutectic carbides, particularly of Fe–Cr rich carbides like $\mathrm{M_{23}C_6}$, during solidification of the liquid phase from the sintering temperature are detrimental for mechanical properties [2]. The avoidance of eutectic reactions provides a further design constraint. Equilibrium solidification paths for various type of HSS alloys are discussed in detail by Halfa [18] with the help of calculated phase diagrams. For example, in M2 type tool steels, the liquid phase at the sintering temperature transforms to either γ or M6C without the formation of deleterious eutectic carbides.

$$\left(\gamma + \mathrm{M_6C} + \mathrm{Liq}\right) \rightarrow \left(\gamma + \mathrm{M_6C}\right) \tag{2}$$

Thus, a microstructural constraint, based on the balance of phase fractions below and above the solidus temperature can be considered to avoid eutectic structures after solidification. Note that this approach is based on equilibrium phase calculations and hence it may have limitations in capturing the realistic solidification scenarios under faster cooling rates. However, design outcomes can always be checked using specialized non-equilibrium solidification simulation tools as discussed in Design Exercise and Results section.

Design Objectives

Processability Factor

The desirable features of HSS alloys for efficient SLPS are often summarized using a systematic phase diagram for a hypothetical system as shown in Fig. 3 [2, 3, 9, 16]. Generally, an alloy can have reduced sensitivity to feedstock and process variabilities if it is solute rich (high X e.g. of carbon), there is a large compositional difference between the lines defining the liquidus and solidus $X_\mathrm{L} - X_\mathrm{s}$, large difference between the liquidus and solidus temperatures $T_\mathrm{L} - T_\mathrm{s}$, lower sintering temperature and steep solidus and liquidus lines or low rate of change of the liquid volume fraction with temperature, dV_L/dT.

Increasing the composition of component X will also enhance mechanical properties by contributing to solution and/or precipitation hardening. Larger $X_\mathrm{L} - X_\mathrm{s}$ and $T_\mathrm{L} - T_\mathrm{s}$

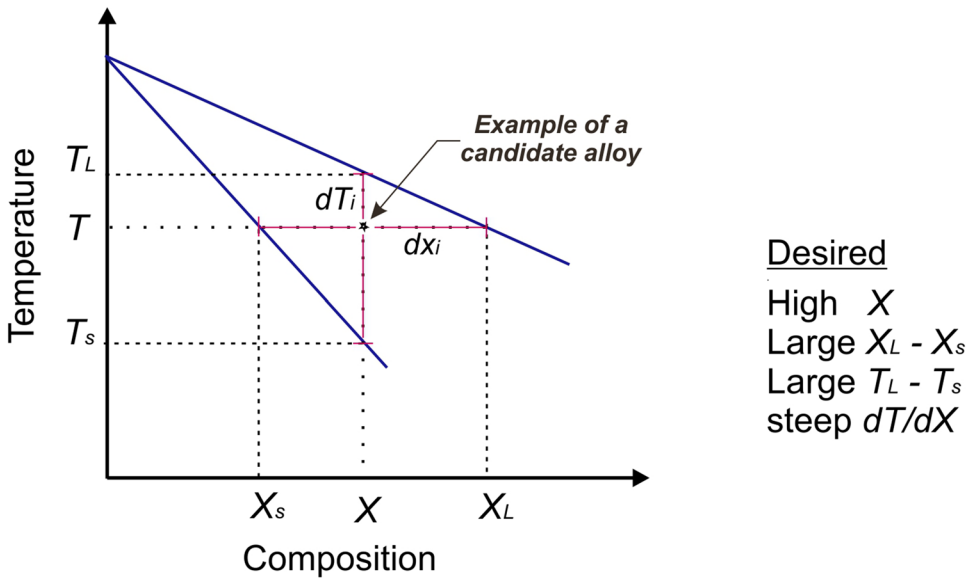

Fig. 3 Schematic phase diagram for hypothetical system showing desirable features required for SLPS [3]

will make the sintering window wider. Minimizing dV_L/dT will make the alloy system robust enough for process variabilities by making temperature control less critical (i.e., if volume fraction of liquid does not change rapidly with temperature). Furthermore, lower sintering temperature, T, reduces the cost of processing. Lower sintering temperature can also reduce grain growth especially in the final stage of sintering.

If the maximum and minimum fractions of the liquid phase required for SLPS are prescribed, then the upper and lower temperature limits, T_L and T_s can be replaced by the temperatures corresponding to the maximum and minimum fractions of the liquid phase, i.e., $T_{f^L_{\max}}$ and $T_{f^L_{\min}}$ respectively.

The set of the desired characteristics can be combined linearly, with equal weights, to formulate a design objective, which represents the processability, *p(X, T)*, of a given alloy as:

$$p(X,T) = X + \left(X_L - X_S\right) + c_t \frac{\left(T_{f^L_{\max}} - T_{f^L_{\min}}\right)}{T\left(\frac{dV_L}{dT}\right)} + \xi, \tag{3}$$

where ξ represents the relative position of the candidate alloy between the liquidus and solidus concentration limits and is given by $\left(X - X_S\right)\left(X_L - X\right)/\left(X_L - X_S\right)$. c_t is a constant to normalize the magnitude of the third term to the order of compositions. The ξ factor increases the p value of alloys close to the mid-point between X_L and X_s compared to alloys close to the phase boundaries. Maximizing p reduces the sensitivity of the alloy to variations in composition and temperature.

Mechanical Property Factor

The other design objective is to either maximize or at least maintain the critical mechanical properties of HSS alloys. The important mechanical properties of HSS alloys include hardness and wear resistance, which are proportional to its strength. The microstructure of heat-treated tool steels consists mainly of a martensitic matrix together with a dispersion of primary and secondary carbides [19]. Thus, the change in yield strength, $\Delta\sigma_y$, of a fully dense tool steel will have contributions from solid solution, $\Delta\sigma_{ssh}$, martensite, $\Delta\sigma_{mrt}$, precipitation, $\Delta\sigma_{ppt}$ and grain boundary, $\Delta\sigma_{gb}$, hardening and can be expressed as [12]:

$$\Delta\sigma_y = \Delta\sigma_{ssh} + \Delta\sigma_{mrt} + \Delta\sigma_{ppt} + \Delta\sigma_{gb}. \tag{4}$$

In the case of PM alloys, the contribution from grain boundary hardening, $\Delta\sigma_{gb}$ is a function of the final grain size after sintering and is barely affected by variations in composition. Thus, for the purpose of alloy design, the change in strength due to solution, martensitic and precipitation hardening can be used as an indicator of hardness and wear resistance. Note that the relative change in strength of the multi-component alloy is considered instead of the absolute strength as the latter requires complex and high-fidelity models. The approach adopted here enables the use of simplified analytical models and thus helps to explore alloy systems without losing a significant amount of information.

Solution hardening arises from the concentrations of both substitutional and interstitial elements in the alloy. The change in strength due to solid solution, $\Delta\sigma_{ssh}$, at an isothermal temperature can be given by:

$$\Delta\sigma_{\text{ssh}} = \sum_{\alpha} f^{\alpha}\left[\sum_{i=1}^{N}\sum_{k>i}^{N} A^{\alpha}_{M_iM_kVa}\left(c'_{M_i}c''_{M_k}\right)^{q}c''_{Va} + \sum_{i=1}^{N}\sum_{j=1}^{n} A^{\alpha}_{M_iI_jVa}\left(c''_{Va}c''_{j}\right)^{r}c'_{M_i}\right], \tag{5}$$

where f^{α} represents the fraction of phase,α. The model considers the effect of substitutional as well as interstitial elements in strengthening or softening on the multi-component material separately. The first summation in the bracket represents strengthening due to addition of substitutional solutes and is performed over N substitutional elements. Thus, $A^{\alpha}_{M_iM_k}$ defines the strengthening parameter when a substitutional element,M_k, is added to M_i. The second summation represents contributions to strengthening due to addition of interstitial solutes and hence it is performed over n interstitial elements. Similarly, $A^{\alpha}_{M_iI_j}$ is a parameter defining strengthening when an interstitial, I_j, is added to substitutional element, M_i. The coefficients, q and r, are often chosen to be 2/3 as per the suggestion from Labusch et al. [20]. The factors c' and c'' represent the concentrations for the substitutional and interstitial elements respectively. By considering the change in the hardness or yield strength of the alloy with respect to changes in concentration of a specific element, the strengthening parameters for the model can be obtained. Further details of the model and the methodologies to determine strengthening coefficients for multi-component alloys can be found in [12, 21].

Martensite hardening in tool steels is due to the transformation of the austenite (γ-FCC) matrix into martensite (α′-BCT) during rapid cooling from the austenization temperature. It occurs through a diffussionless displacive transformation causing lattice distortion by carbon atoms and creating barriers to dislocation motion. It has been shown that martensite hardening is proportional to dislocation length *(L)* and concentration of carbon *(x_c)* [19] and can be given by:

$$\Delta\sigma_{\text{mrt}} = K_{\text{m}}(L)^{-\frac{1}{2}}\left(x_c\right)^{\frac{1}{3}}, \tag{6}$$

where K_m is a constant. Equation (6) implies that martensite strengthening is directly proportional to the concentration of carbon in the alloy.

In the case of tool steels, carbide particles that precipitate during tempering (secondary carbides mainly of MC and M_2C types) are incoherent and deformation occurs with dislocations bowing between particles [19]. Thus, the change in strength due to precipitation hardening,$\Delta\sigma_{\text{ppt}}$, can be estimated using the Ashby-Orwan [22] relationship for multi-component alloys with rigid particles as:

$$\Delta\sigma_{\text{ppt}} = 0.54G_mB\left(\frac{f_p^{\frac{1}{2}}}{X_p}\right)\ln\left(\frac{X_p}{2B}\right), \tag{7}$$

where G_s is the shear modulus of the matrix phase, B is the Burgers vector of the dislocation, f_p and X_p are the volume fraction and mean diameter of precipitate particles respectively. The magnitude of the Burger's vector (B) can be determined as $B = l^p\Big/\sqrt{2}$ where l^p is the lattice parameter of the matrix phase at equilibrium, which can be obtained by using its molar fraction, V_m and Avogadro number, N_A as $l^p = \left(4V_m/N_A\right)^{\frac{1}{3}}$ [10]. Equation (7) shows that precipitation hardening in tool steels increases with the fraction of secondary carbides, which can be estimated by using thermodynamic calculations.

For the purpose of alloy design, material or chemistry related factors from the martensite and precipitation hardening can be considered to formulate a reduced order model *($\Delta\sigma_r$)* for the change in strength of tool steels as:

$$\Delta\sigma_{\text{r}} = \Delta\sigma_{\text{ssh}} + x_c + f_c^{II}, \tag{8}$$

where, $\Delta\sigma_{\text{ssh}}$ is the contribution of solution hardening as given by Eq. (5) and is a function of the concentration of all the components in the alloy, x_c represents the concentration of carbon in the matrix after tempering and reflects the contribution of martensite strengthening and f_c^{II} is the volume fraction of secondary carbides (mainly MC and M_2C types) and accounts for the contribution of precipitation hardening after tempering of the tool steel.

The other important performance requirement of these steels is tool life under thermal and mechanical loading conditions which requires both a high strength matrix phase and blocky or primary carbides [23]. The blocky carbides contribute not only to the tool life but also affects the hardness. The tool life is determined by the wear resistance, which increases with the volume fraction of undissolved (primary) carbides [23]. A higher fraction of primary carbides is also beneficial for coarsening resistance during secondary heat treatment as well as plastic blunting (toughness), which can be described by composite strengthening. Thus, another model can be considered for hardness of tool steels by incorporating the role of volume fraction of primary carbides, f_c^I as:

$$\Delta h_{\text{r}} = \Delta\sigma_{\text{ssh}} + x_c + f_c^I + f_c^{II}. \tag{9}$$

In general, Fig. 4 summarizes the design considerations based on the process-microstructure-property relationships.

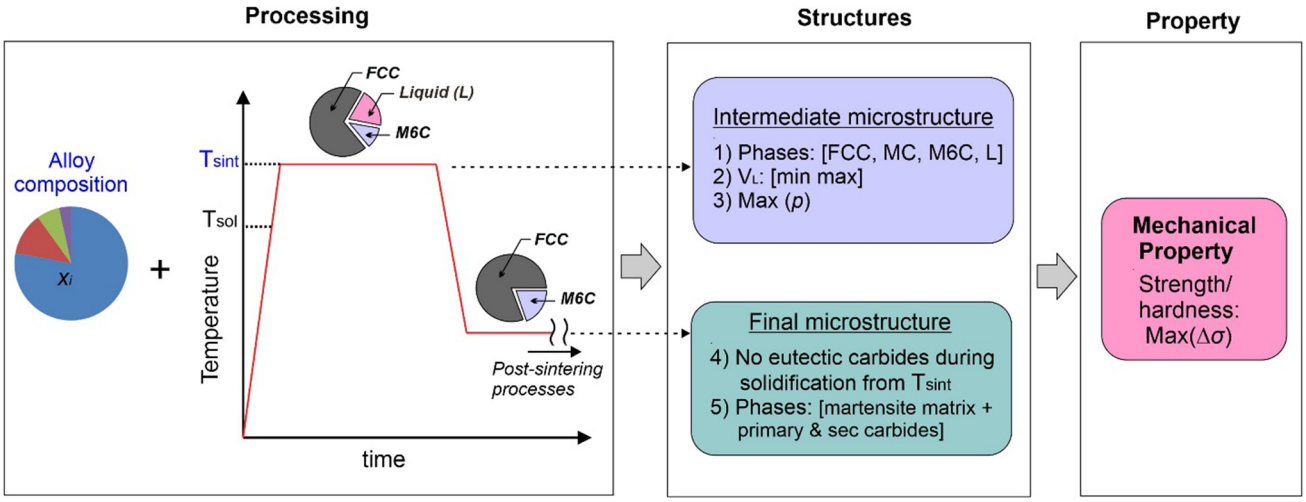

Fig. 4 Schematics showing the relationship between processing and microstructures during sintering of HSS alloys

A design variable constitutes composition (x_i) of alloying elements. The sintering temperature–time profile is assumed to be defined by a constant heating rate to T_{sint} and holding time, t. For every alloy candidate, microstructural attributes, shown in the 'Structures' box, corresponding to the intermediate and final states are calculated. A search algorithm is then developed to identify alloys that fulfill the microstructural constraints followed by optimizing them for maximizing the objectives, i.e., processability (p) and strength ($\Delta\sigma$).

Computational Design Methods

The computational design methodology involves a multi-objective optimization of the composition of the HSS alloy system. It consists of an evolutionary (genetic) algorithm, which generates and evaluates candidate alloys based on feedback from (i) computational thermodynamics for microstructural conditions at sintering (Eq. 3) and (ii) reduced order mechanical property models (Eqs. 8 and 9).

Computational Thermodynamics

Thermodynamic computations were carried out using Thermo-Calc (TC), a commercial software based on the CalPhaD method [24]. Thermodynamic database for iron-based alloys, TCFE9, was used and results were accessed through Python using the TC-Python interface.

The sintering temperature of an alloy with a given composition is determined as follows. First the lower and upper bounds of temperatures (T_1 and T_2) corresponding to the minimum and maximum volume fraction of liquid phase for SLPS are calculated. Then, the sintering temperature is randomly chosen between T_1 and T_2. This ensures the alloy has the necessary amount of liquid phase at the sintering temperature. The phase fractions of candidate alloy systems at the required temperature are calculated by TC using single point equilibrium calculations, which is used to select alloy candidates that satisfy the necessary criterion discussed in Design Considerations section.

The change in the volume fraction of the liquid phase with temperature, dV_L/dT of a given alloy is obtained by extracting the volume fraction of the liquid, V_L at a set of temperatures defined by $T_i = T + dT_i$, where i increases for a few number of data points, see Fig. 3. The slope of a linear fitting between V_L and T_i data is then considered to be equal to dV_L/dT.

The compositional limits defining the sintering window (see Figs. 2 and 3) are calculated from a 2D section of the phase diagram by considering the left and right boundaries of the FCC + M6C + Liq field at the sintering temperature. Note that unlike the hypothetical phase diagram shown in Fig. 3, the lines defining the boundaries of the sintering window in HSS systems may not be described explicitly by the liquidus and solidus. Instead, the boundaries of the region that consists of the required phases, FCC + M6C + Liq, are identified during the calculation of the compositional limits.

Theoretically, the sintering window of a multi-component alloy should be quantified across multiple 2D sections of the phase diagram considering the pseudo binary plots of T *vs* x_i where x_i is the alloying element. This would require describing the processability factor by a vector with components calculated based on the different sections corresponding to each of the alloying elements. However, for tool steels, the sintering window is often described by a pseudo binary section of T *vs* x_c where

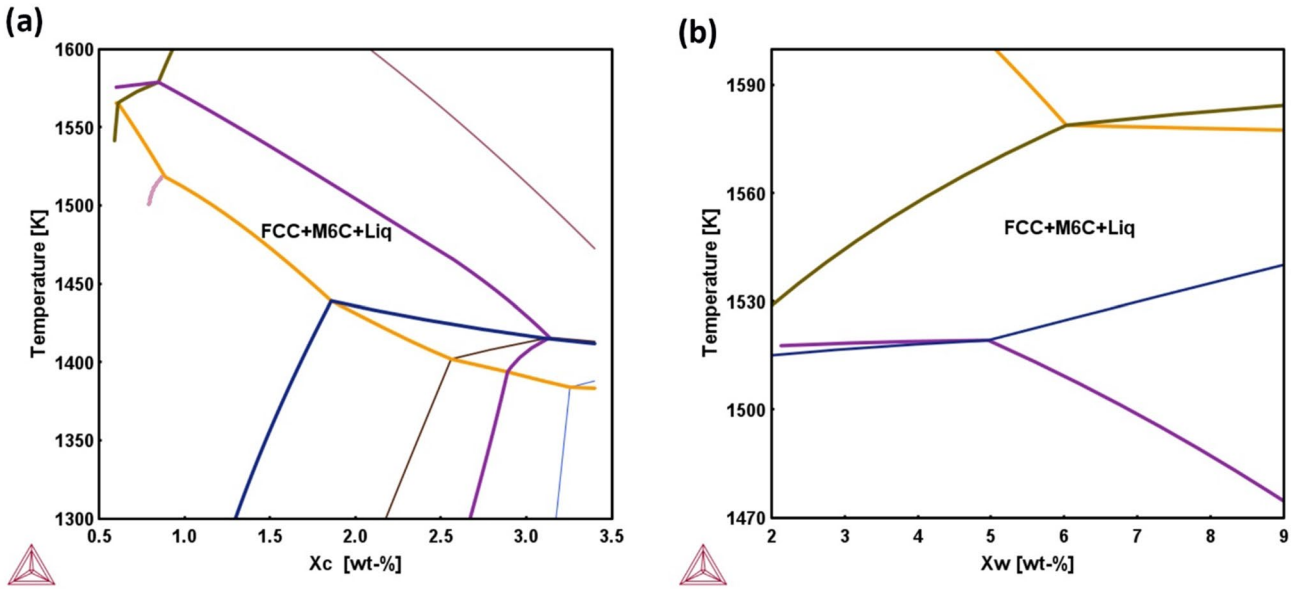

Fig. 5 Calculated phase diagram of M2 steel (Fe-0.8C-6 W-5Mo-4Cr-2 V) using **a** T–X_c and **b** T–X_W sections

x_c is the concentration of carbon [2, 3, 25, 26]. Because the FCC + M6C + Liq field becomes narrow across the T *vs* x_c dimension, this section is critical for improving the processability. Figure 5 shows the sintering window of M2 (Fe-0.8C-6 W-5Mo-4Cr-2 V) using two pseudo-binary sections of the phase diagram demonstrating a narrow compositional limit of the FCC + M6C + Liq field across the T *vs* x_c section.

Furthermore, it is critical to reduce the sensitivity of tool steels to variation in carbon concentration, which often occurs not only during feedstock preparation but also due to the residual carbon from the de-binding process. The concentration of carbon also controls carbide formation during secondary heat treatment cycles affecting the final mechanical properties.

Optimization Using Genetic Algorithm

The non-dominated sorting genetic algorithm (NSGA-II) [27] was used to carry out the multi-objective optimization. The NSGA-II provides a set of non-dominated solutions, which are known as a Pareto set. In the NSGA-II, each alloy system is considered as a chromosome having genes representing the percentage by weight of alloying elements. The population of these chromosomes evolves through varying the values of the genes according to their fitness to the objective function. Figure 6 shows the flowchart of the algorithm used in the computational design optimization of HSS alloys.

Non-dominated sorting is performed in a way to choose alloy systems with acceptable solutions, i.e., those with higher processability and mechanical properties. Finally, results of the alloy systems in the Pareto frontier for both objectives are determined. In this way, bottom-up information flow is combined with top-down search based on processing and/or performance requirements in the presence of uncertainty.

Details of the NSGA-II employed in this study can be summarized as follows:

(1) An initial set of N_p individual candidates (chromosomes) with all the design variables (genes) consisting of the weight percentage of *alloying elements* (x_i) are generated randomly within a predefined minimum and maximum bounds.
(2) For the first iteration, the population (pop) will be made up of parents involving all the initial candidates generated in Step 1.
(3) For each of the candidates, single point equilibrium calculations are performed to determine the temperatures T_1 and T_2 corresponding to the pre-defined minimum (V_{min})and maximum (V_{max}) volume fraction of the liquid phase for SLPS. The sintering temperature is then selected between T_1 and T_2.
(4) Alloys are then checked for all the microstructural constraints discussed in Microstructural Constraints section.
(5) For those candidates that satisfy the condition in step 4 (e.g., M_p candidates where $M_p <= N_p$), the objective functions i.e., the processability (p) and change in strength and hardness are calculated.

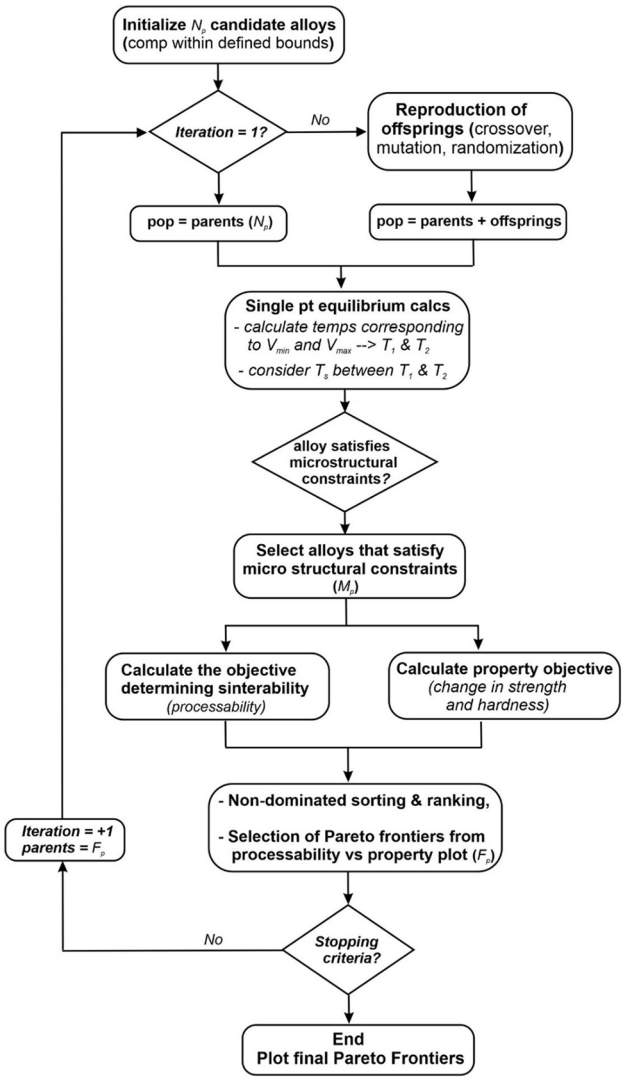

Fig. 6 Flowchart showing the design optimization procedures

(6) Non-dominated sorting of the M_p candidates are then performed using ranking and crowding distance techniques [28]. Sorting of the candidates is performed based on maximizing both processability and the mechanical properties.

(7) Selection of the best candidates, for example the frontiers (F_p) of the Pareto solutions, are considered for next iteration.

(8) If the stopping criteria is not achieved, off-spring population is generated through GA reproduction techniques (i.e., crossover and mutation) using the best set of individuals (parents) selected from the previous iteration.

(9) The population (pop) for the next cycle will be assembled using both the parents (from previous cycle) and off-springs (from the reproduction step).

(10) To diversify the pool of candidates in every reproduction step, a new set of randomly generated individuals, about 10% of the initial population, are added. This enhances the search performance by diversifying the solution space and helps to avoid convergence to local optima.

(11) The iteration continues until the stopping criteria is achieved, which can be determined based on the improvements of the objective functions. Example, the stopping criteria can be based on iteration number after which no improvements (movement of the Pareto front) are observed.

Verification of Design Models

Processability Model

Verifying the predictive capability of the processability model discussed in section Design Objectives is important before using it in the design exercise. This is performed by comparing the predicted processability values with that of experimental observations performed by Wright et al. [2] for various HSS alloys. Table 1 summarizes the comparisons based on the alloy codes used in the reference work together with the authors comments after sintering at different

Table 1 Comparison of experimental observations with the model predictions in the current study

Alloy code as per Ref. [2]	Optimal sintering temperature (°C)	Comments by Wright et al. [2] after exp observations	Processability as per the current study
P1A	1180	Unsinterable, eutectic structures present	Do not satisfy microstructure constraints at T_{sint}
P2A	1230	Sinterable alloy	Sinterable with $p = 0.030$
P2B	1210	Sinterable alloy	Sinterable with $p = 0.034$
P2C	1200	Highly sinterable alloy	Sinterable with $p = 0.040$
P3A	1200	Highly sinterable alloy	Sinterable with $p = 0.038$
P4A	1240	Limited sinterability	Do not satisfy microstructure constraints at T_{sint}
P5A	1210	Highly sinterable alloy	Sinterable with $p = 0.037$
P5B	1175	Highly sinterable alloy	Sinterable with $p = 0.042$

temperatures. It is found that the calculated processability (p) values agree well with the experimental observations (comments) for all the alloys, demonstrating the capability of the model.

Mechanical Property Model

The contribution of solution hardening should be evaluated based on the concentrations of solutes in the matrix after secondary heat treatment (tempering) cycles. Determination of solutes in the matrix requires simulating the precipitation process, for example by using TC-Prisma [29], at tempering temperatures. On the other hand, the change in strength due to precipitation hardening should be estimated by considering the fraction of secondary carbides after tempering. This is because precipitation hardening in HSSs is often caused by secondary carbides (mainly MC and cubic M_2C) that nucleate and grow during the tempering cycles [19].

Karagoz and Fischmeister [23] demonstrated that the formation of secondary carbides during tempering of tool steels results in significant depletion of the solutes in the solid solution matrix. This will obviously reduce the contribution of solution hardening to strengthening of the matrix. To demonstrate the relative contributions of solution and precipitation hardening in tool steels, Eqs. (5) and (7) are used together with data for the concentration of solutes in the matrix (after tempering) and the fraction of secondary carbides reported in ref [23]. For the sake of comparison, the mean precipitate size of 50 nm and shear modulus of 100 GPa are assumed to evaluate the precipitation hardening. Six PM alloys from ref [23] are divided into three groups depending on the similarity of their heat treatment cycles, see Table 2. Data for M2 tool steel, which is considered as a reference alloy in our design exercise—section Design Exercise and Results, is also provided.

The results in Table 2 show that the relative contribution of solution hardening is very small compared to precipitation hardening due to very low concentrations of solutes in the matrix. This is consistent with the conclusion of El-Rakayby [19] that strength in tool steels is controlled primarily by precipitation of secondary carbides. In addition, the fact that the measured hardness is almost the same for all G2 alloys (despite variations in their compositions) also indicate that the hardness may have been affected by primary carbides (which is the same for all the alloys) in addition to secondary carbides.

Though simplified assumptions are used, the results in Table 2 imply that the reduced models in Eqs. (8) and (9) for change in strength ($\Delta\sigma_r$) and hardness (Δh_r) can be simplified further as:

$$\Delta\sigma_r = x_c + f_c^{II} \tag{10}$$

$$\Delta h_r = x_c + f_c^{I} + f_c^{II} \tag{11}$$

Comparison of measured bend strength and hardness data for various types of tool steels with the reduced models in Eq. (10) are performed. Figure 7a shows the bend strength of various PM tool steels reported by Wright et al. [3] increasing with the model ($\Delta\sigma_r$) as shown by the trend line except for one of the data points with a larger error bar. In addition, Fig. 7b also shows the normalized hardness data for different tool steels, from refs [23, 30–33], increasing with the corresponding normalized Δh_r. The normalized values, x_n for a data set, x are calculated as: $x_n = \left(x_i - x_{\min}\right)/\left(x_{\max} - x_{\min}\right)$. Note that the reduced order models capture material related effects, and they primarily show the trend in the variation of the properties as a function of composition. Therefore, the results in Fig. 7a, b demonstrate that the models can be used as proxy to compare and choose (design) alloys for enhanced mechanical properties.

Note that for a given alloy, the amount (fraction) of primary carbides can be determined after a single point equilibrium calculation at the austenization temperature. On the

Table 2 Relative comparison of solution and precipitation hardenings in tool steels

Group	Alloy as per the name in Ref. [23]	Austenization temperature (°C)	Fraction of primary carbides (vol %) Ref. [23]	Fraction of secondary carbides (vol %) Ref. [23]	Measured hardness (HRC), Ref. [23]	Change in strength [MPa] from models	
						$\Delta\sigma_{ppt}$	$\Delta\sigma_{ssh}$
G1	PM/M2mod	1210	11.3	2.01	65	181	19
	PM/T15mod	1210	11.7	3.91	67	251	28
G2	PM/exp Nb + 3Co	1230	5.4	3.02	65.5	225	16.5
	PM/exp Nb + 5Co	1230	5.4	3.02	66	225	16.3
	PM/exp Nb + 8Co	1230	5.4	2.91	66.5	221	17.1
G3	PM/exp Nb	1230	5.4	3.15	64.5	230	14.2
	M2	1220	6.8	3.00	65	224	18.0

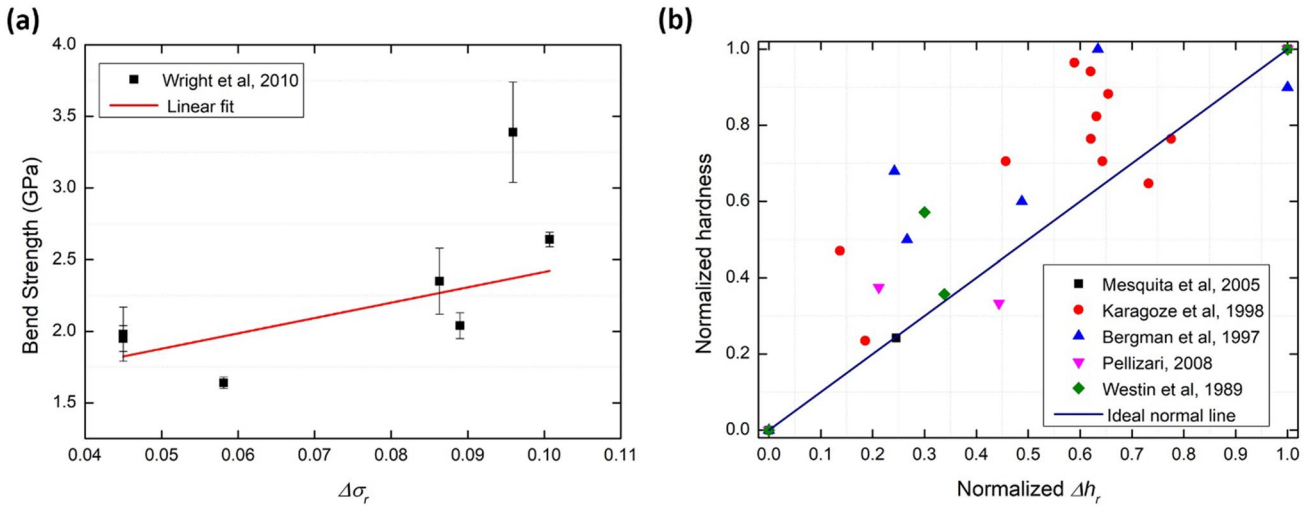

Fig. 7 Comparison of measured data with the reduced models for change in strength and hardness: **a** bend strength and **b** hardness

Table 3 The nominal compositions (wt %) of M2, T42, and M35MHV together with the upper and lower composition bounds for the design exercise

Design variables (wt-%)	M2	T42	M35MHV	Variable bounds	
				Min	Max
C	0.85	1.3	1.8	0.8	2.4
W	6.0	9.0	6.0	1.0	12.0
Mo	5.0	3.0	5.0	3.0	14.0
Cr	4.0	4.0	4.0	4.0	5.0
V	2.0	3.0	4.0	1.0	6.0
Co	–	9.0	5.5	0.0	12.0
Fe	Bal	Bal	Bal	Bal	Bal

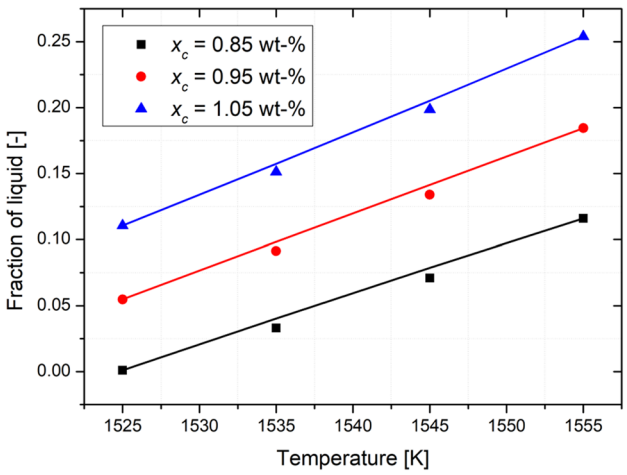

Fig. 8 Change in molar fraction of liquid phase with temperatures at different concentrations of carbon

other hand, the fraction of secondary carbides is determined by subtracting primary carbides from the total fraction of carbides after tempering [34]. The capability of thermodynamic simulations using TCFE database for predicting the fraction of carbides in HSS alloys is demonstrated by Halfa et al. [18] and Wright et al. [2] by comparing with experimental measurements.

Design Exercise and Results

The design framework developed in this study is used to perform design of Tungsten (W) and Molybdenum (Mo) based HSS alloy by using the minimum and maximum range/bounds for each of the design variables as shown in Table 3. The concentrations for each of the alloying elements vary between the minimum (Min) and maximum (Max) limit. These limits are selected considering the various commercial HSS alloys as a reference and can be modified. The sintering temperature for each of the candidate alloy is determined as per the procedure described in Optimization Using Genetic Algorithm section. In addition, the reduced model for mechanical properties, Eqs. (10) and (11) are implemented by using austenization and tempering temperatures of 1413 K and 813 K respectively. These values are selected based on the common practice for secondary heat treatments of tool steels [23] and they can be modified.. The optimal alloys determined in this study are compared with the standard M2 alloy with the nominal compositions shown in Table 3 [3]. The optimal sintering temperature for M2 is suggested to be 1533 K [26], which is used to evaluate its processability. Two other standard alloys with medium and high carbon

concentrations, T42 and M35MHV respectively, are also considered to compare with the solutions from this study, see Table 3.

A key parameter in the processability factor is the change in the volume fraction of the liquid phase with temperature, dV_L/dT. Figure 8 shows the variation of the fraction of liquid as a function of temperature for M2 (which has $X_c = 0.85$ wt-%) and another two alloy systems where only the composition of carbon is increased to $X_c = 0.95$ and 1.05 wt-%. The change in the molar fraction of the liquid with temperature is found to increase in a linear manner in all cases and hence the calculated data points are shown together with the corresponding linear fit. The slope, dV_L/dT, for M2 is evaluated to be 0.35 [%/K]. At the optimal sintering temperature ($T_{opt} = 1533\ K$), it was also found that the fraction of the liquid phase varies significantly with the concentration of carbon and the processability *(p)* value is calculated to be 0.024.

Figure 9a, b show the Pareto solutions from the design optimization, i.e., $\Delta\sigma_r$ versus p and Δh_r versus p respectively. A point in each of the Pareto-frontiers corresponds to a unique alloy defined by composition and optimal sintering temperature. All the points in the Pareto-frontier are optimal in the sense that one objective cannot be improved without compromising the other. Thus, the choice of the 'best' point from the Pareto-set depends on the users' priority.

Three separate optimizations were performed by considering initial population size of 100 with crossover and mutation probabilities of 0.8 and 0.1, respectively. The resulting solutions from the three optimizations are found to converge to the same frontier. In addition, the outward movement of the frontiers (i.e., improvement of solutions) stabilized after the 40th iteration and hence a limit of 50 iterations was used as a stopping criterion. The optimizations required an average computational time of 34 h on a virtual machine consisting of 12 CPU cores.

Results corresponding to M2, M35MHV and T42, assuming a sintering temperature of 1533 K, are also shown in Fig. 9a, b. Figure 9 demonstrates that it is possible to identify alloys with significantly better processability (p) and improved mechanical properties compared to standard alloys. The contour plot of the Pareto surface where the process factor is plotted as a function of the mechanical property indicators (i.e., $\Delta\sigma_r$ and Δh_r) is shown in Fig. 10. Processability decreases with improvement in mechanical properties indicating that it is difficult to maximize mechanical properties and processability contemporaneously. Note that in the current study, toughness and hot strength have not been considered while evaluating the mechanical properties. Obviously, incorporating these properties into the property design criteria would make the design more comprehensive.

Table 4 shows the composition (wt-%) and sintering temperature (Kelvin) for three optimal alloys with the largest $\Delta\sigma_r$ (New-A), largest Δh_r (New-B) and largest processability (New-C), see Fig. 9a, b. It is shown that the alloy with the largest processability factor (New-C) has the lowest sintering temperature. The alloy with the highest hardness (New-A) still requires the highest sintering temperature.

Note that molybdenum (Mo) in HSS alloys forms the same double carbide with iron and carbon as tungsten does and it can be substituted for tungsten (W) on the basis of approximately one part of molybdenum, by weight, for two parts of tungsten [35]. On this basis, the composition of New-C can be approximately regarded as Fe–14Mo–5Co–4.7Cr–1.3C. This composition is quite similar to the HSS alloy (Fe–14Mo–8Co–4Cr–1.3C) reported by Wright et al. [2] that showed less sensitivity to material

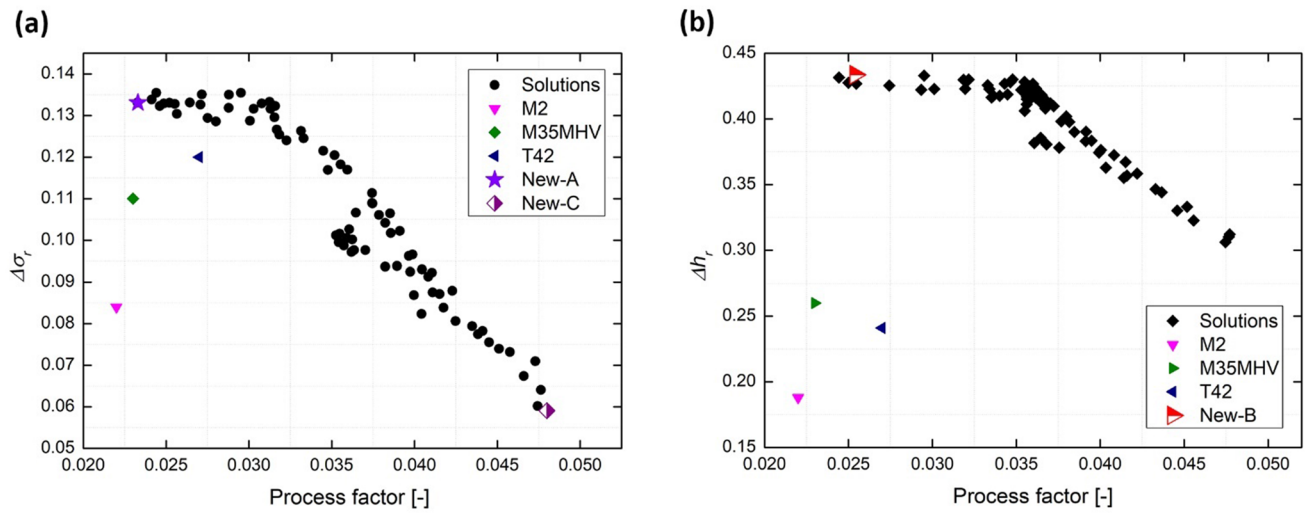

Fig. 9 Pareto frontier of optimal solutions showing change in strength versus processability: **a** change in strength versus processability and **b** change in hardness versus processability

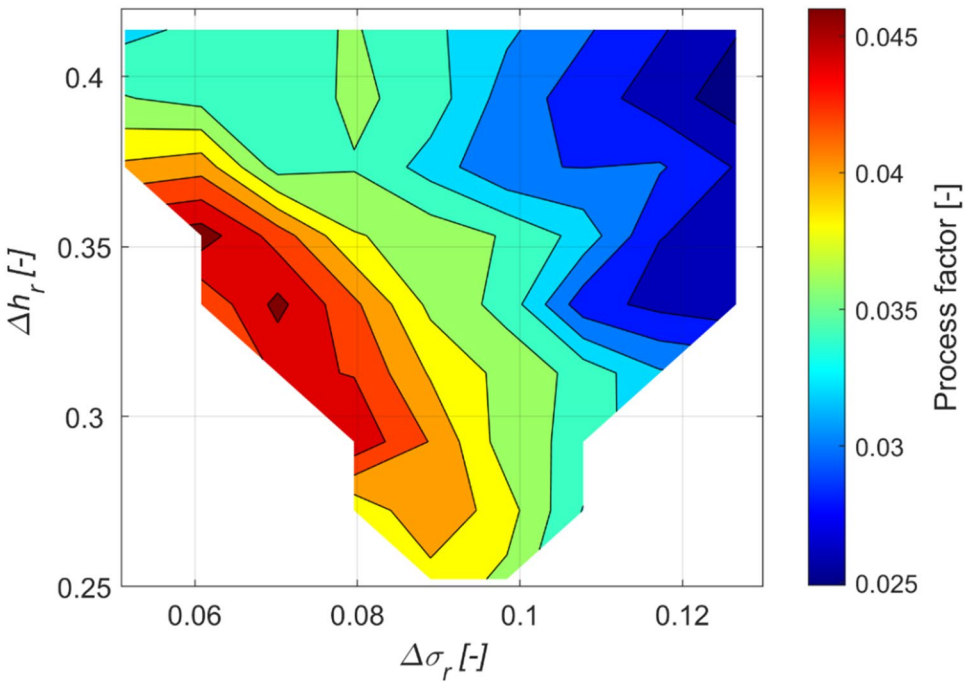

Fig. 10 Contour plot of process factor as a function of strength and hardness

Table 4 Optimal compositions and sintering temperatures of alloys for the three representative solutions shown in Fig. 9a, b

Alloy	Fe	C	W	Mo	Cr	V	Co	T_{opt}
New-A	Bal	1.11	10.91	6.24	4.93	4.60	6.34	1534
New-B	Bal	2.17	10.14	13.31	4.81	4.59	2.88	1496
New-C	Bal	1.35	10.42	9.00	4.71	1.63	5.13	1491

Table 5 Comparison of the optimal alloys with M2 in terms of the desired features for efficient SLPS

Criteria	Standard M2	New-A	New-B	New-C
X_L—X_s [wt %]	0.73	1.43	0.95	1.57
T_L—T_s [K]	50	65	65	120
dV_L/dT [%/K]	0.35	0.40	1.10	0.27
T_{sint} [K]	1533	1534	1496	1491

as well as process variabilities. This agreement, once again, validates the effectiveness of the design method.

Improvements of the optimal alloys in terms of the desired characteristics discussed in section Design Objectives are summarized in Table 5 in comparison to the standard M2. Processability can be shown in terms of the optimum sintering temperature (T_{sint}), the sintering window (the range of composition and temperatures over which acceptable microstructures and properties are obtained) [3]. Alloys can be considered to have enhanced processability or sinterability, if T_{sint} and dV_L/dT are lower together with wider sintering window than those for current grades. Table 5 shows that the optimal alloy with the maximum process factor (New-C) has significant improvement in all the desired characteristics. Once again, these results demonstrate that it is possible to identify alloy compositions with better sinterability in terms of the desired features for SLPS of HSS powder compacts.

The presence of an eutectic transformation and carbides like $M_{23}C_6$ during solidification from the sintering temperature are deleterious for mechanical properties of HSS alloys [2]. It is therefore important to verify the solidification behavior of the liquid phase at the sintering temperature under realistic cooling rates. For this purpose, the Scheil–Gulliver non-equilibrium solidification calculation module available in Thermo-Calc is used together with the compositions for the three alloys shown in Table 4. The non-equilibrium solidification behavior for the three alloys are simulated by setting their respective sintering temperature, see Table 4, as the initial condition and a cooling rate of 1.0 K/s to mimic the reality. The simulation is run until the fraction of liquid in the systems reaches close to zero (1e-4 vol-%). Figure 11 demonstrates the temperature versus fraction of solid phases curves obtained from Scheil–Gulliver non-equilibrium solidification calculations for the three alloys (New-A, New-B and New-C). All the three alloys show a similar solidification behavior with the last liquid, as shown by the last segment of the solidification curves, expected to solidify without eutectic reaction. Furthermore, the unnecessary carbide like $M_{23}C_6$ has not been observed, demonstrating

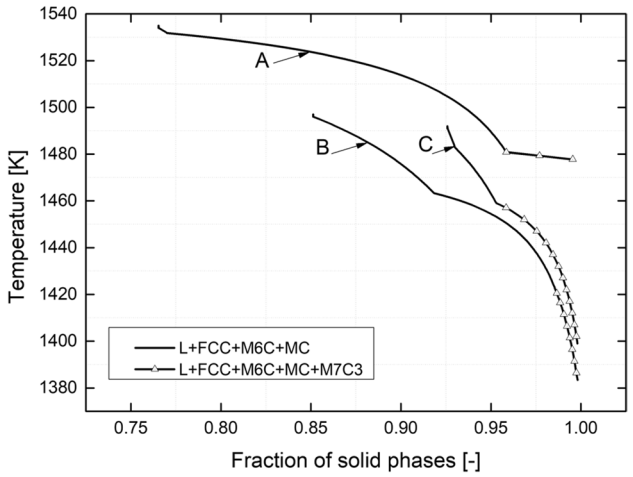

Fig. 11 Temperature versus mole fraction of solid phases, A, B, C refer to New-A, -B and -C respectively. The final solidification reaction in all three alloys do not show formation of eutectic or $M_{23}C_6$ carbides

once again, the capability of the design method developed in this study.

Conclusion

Computational design methods for materials should address uncertainties in materials as well as process variabilities that may occur during manufacturing. In this study, an ICME framework was developed for designing multi-component alloys that are sensitive to feedstock and process-related variabilities during their processing cycles. To facilitate the design, reduced order design models were developed, and their performance was validated using data from the literature. The capability of the algorithm is demonstrated by designing HSS alloys processed by PM routes involving SLPS. The design exercise aimed to improve processability of HSS alloys using PM routes by focusing primarily on integrating processing (composition, controllability) with the structure (microstructural phases) and with critical properties (strength and hardness). This demonstrates that it is possible to identify unique alloy compositions which have reduced sensitivity to variation in material (composition) and process conditions (sintering temperature) and that also have improved mechanical properties, compared to conventional commercial alloys.

Funding Open Access funding enabled and organized by CAUL and its Member Institutions.

Declarations

Conflict of interest On behalf of all authors, the corresponding author states that there is no conflict of interest.

References

1. Taguchi G (1993) Taguchi on robust technology development: bringing quality upstream. ASME Press, New York
2. Wright CS, Youseffi M, Wronski AS, Ansara I, Durand-Charre M, Mascarenhas J, Oliveira MM, Lemoisson F, Bienvenu Y (1999) Supersolidus liquid phase sintering of high speed steels: part 3: computer aided design of sinterable alloys. Powder Metall 42:131–146. https://doi.org/10.1179/003258999665486
3. Wright CS, Wronski AS, Iturriza I (2000) Development of robust processing routes for powder metallurgy high speed steels. Mater Sci Technol 16:945–957. https://doi.org/10.1179/026708300101508793
4. Liu Z, Loh N, Khor K, Tor S (2000) Sintering of injection molded M2 high-speed steel. Mater Lett 45:32–38. https://doi.org/10.1016/S0167-577X(00)00070-7
5. Kulkarni KM (1990) Liquid phase sintering in high speed steels. Met Powder Rep 45:629–633. https://doi.org/10.1016/0026-0657(90)90594-7
6. Várez A, Levenfeld B, Torralba J, Matula G, Dobrzanski L (2004) Sintering in different atmospheres of T15 and M2 high speed steels produced by a modified metal injection moulding process. Mater Sci Eng A 366:318–324. https://doi.org/10.1016/J.MSEA.2003.08.028
7. Lumley RN, Schaffer GB (1998) The effect of additive particle size on the mechanical properties of sintered aluminium-copper alloys. Scr Mater 39:1089–1094. https://doi.org/10.1016/S1359-6462(98)00278-4
8. Lumley RN, Schaffer GB (1996) The effect of solubility and particle size of liquid phase sintering. Scr Mater 35:589–595. https://doi.org/10.1016/1359-6462(96)00195-9
9. German RM (1997) Supersolidus liquid-phase sintering of prealloyed powders. Metall Mater Trans A 28:1553–1567. https://doi.org/10.1007/s11661-997-0217-0
10. Li S, Kattner UR, Campbell CE (2017) A computational framework for material design. Integr Mater Manuf Innov 6:229–248. https://doi.org/10.1007/s40192-017-0101-8
11. Deschamps A, Tancret F, Benrabah IE, De Geuser F, Van Landeghem HP (2018) Combinatorial approaches for the design of metallic alloys. Comptes Rendus Phys 19:737–754. https://doi.org/10.1016/j.crhy.2018.08.001
12. Molla TT, Liu JZ, Schaffer GB (2018) An ICME framework for design of stainless steel for sintering. Integr Mater Manuf Innov 7:136–147. https://doi.org/10.1007/s40192-018-0115-x

13. Molla TT, Liu JZZ, Schaffer GBB (2019) Computational design of functionally graded materials from sintered powders. Integr Mater Manuf Innov 8:82–94. https://doi.org/10.1007/s40192-019-00127-6
14. Olson GB (1997) Computational design of hierarchically structured materials. Science 277:1237–1242. https://doi.org/10.1126/science.277.5330.1237
15. Hoyle G (1988) High speed steels. Butterworths, London
16. German RM (n.d.) An update on the theory of supersolidus liquid phase sintering. http://www.cavs.msstate.edu/publications/docs/2003/07/2003-15.pdf. Accessed 4 Sept 2019
17. Momeni H, Shabestari S, Razavi SH (2020) Densification and shape distortion of the Al-Cu-Mg pre-alloyed powder compact in supersolidus liquid phase sintering process. Iran J Mater Sci Eng 17:87–92. https://doi.org/10.22068/IJMSE.17.4.87
18. Halfa H (2013) Thermodynamic calculation for silicon modified AISI M2 high speed tool steel. J Miner Mater Charact Eng 01:257–270. https://doi.org/10.4236/jmmce.2013.15040
19. El-Rakayby AM, Mills B (1988) On the microstructure and mechanical properties of high-speed steels. J Mater Sci 23:4340–4344. https://doi.org/10.1007/BF00551928
20. Labusch R (1970) A statistical theory of solid solution. Phys Status Solidi B 41:659–669
21. Walbrühl M, Linder D, Ågren J, Borgenstam A (2017) Modelling of solid solution strengthening in multicomponent alloys. Mater Sci Eng A 700:301–311. https://doi.org/10.1016/j.msea.2017.06.001
22. Gladman T (1999) Precipitation hardening in metals. Mater Sci Technol 15:30–36. https://doi.org/10.1179/026708399773002782
23. Karagöz S, Fischmeister HF (1998) Cutting performance and microstructure of high speed steels: contributions of matrix strengthening and undissolved carbides. Metall Mater Trans A 29:205–216. https://doi.org/10.1007/S11661-998-0173-3
24. Perrut M (2015) Thermodynamic modeling by the calphad method and its applications to innovative materials. J AerospaceLab 9:1–11
25. Wright CSS, Wronski ASS, Iturriza I (2000) Overview: development of robust processing routes for powder metallurgy high speed steels. Mater Sci Technol 16:945–957. https://doi.org/10.1179/026708300101508793
26. Wright CS, Ogel B (1993) Supersolidus sintering of high speed steels: part 1: sintering of molybdenum based alloys. Powder Metall 36:213–219. https://doi.org/10.1179/pom.1993.36.3.213
27. K Deb (2011) Multi-objective optimization using evolutionary algorithms: an introduction. http://www.iitk.ac.in/kangal/deb.htm. Accessed 1 May 2018
28. Shukla PK, Deb K (2006) On finding multiple Pareto-optimal solutions using classical and evolutionary generating methods. Eur J Op Res. https://doi.org/10.1016/j.ejor.2006.08.002
29. Jin S, Chen Q, Bratberg J (2015) Thermodynamic calculations and precipitation simulations of HSLA steels. In: 7th international conference on high strength low alloy steels, vol 1. John Wiley and Sons Inc., pp 173–177. https://doi.org/10.1007/978-3-319-48767-0_16
30. Mesquita RA, Barbosa CA (2005) High-speed steels produced by conventional casting, spray forming and powder metallurgy. Mater Sci Forum. https://doi.org/10.4028/www.scientific.net/msf.498-499.244
31. Bergman F, Hedenqvist P, Hogmark S (1997) The influence of primary carbides and test parameters on abrasive and erosive wear of selected PM high speed steels. Tribol Int. https://doi.org/10.1016/S0301-679X(96)00040-0
32. Pellizzari M (2008) Influence of deep cryogenic treatment on the properties of conventional and PM high speed steels. Metall Ital 100(8):17–22
33. Westin L (1989) Mechanical properties of PM high-speed steels related to heat treatment and hardness. Met Powder Rep 44:768–773
34. Henderer WE (1979) Strengthening mechanisms in high-speed steel as related to tool-life. J Manuf Sci Eng Trans ASME 101:217–222. https://doi.org/10.1115/1.3439498
35. AM Bayer, BA Becherer, T Vasco (1989) High speed tool steels, ASM Handb. 16:51–59. https://www.asminternational.org/documents/10192/1849770/06022g_sample.pdf. Accessed 14 Dec 2020